ORIGINAL ARTICLE

Finite element analysis of the influence of loading rate on a model of the full lumbar spine under dynamic loading conditions

Eric Wagnac · Pierre-Jean Arnoux ·
Anaïs Garo · Carl-Eric Aubin

Abstract Despite an increase in the number of experimental and numerical studies dedicated to spinal trauma, the influence of the rate of loading or displacement on lumbar spine injuries remains unclear. In the present work, we developed a bio-realistic finite element model (FEM) of the lumbar spine using a comprehensive geometrical representation of spinal components and material laws that include strain rate dependency, bone fracture, and ligament failure. The FEM was validated against published experimental data and used to compare the initiation sites of spinal injuries under low (LD) and high (HD) dynamic compression, flexion, extension, anterior shear, and posterior shear. Simulations resulted in force–displacement and moment-angular rotation curves well within experimental corridors, with the exception of LD flexion where angular stiffness was higher than experimental values. Such a discrepancy is attributed to the initial toe-region of the ligaments not being included in the material law used in the study. Spinal injuries were observed at different initiation sites under LD and HD loading conditions, except under shear loads. These findings suggest that the strain rate dependent behavior of spinal components plays a significant role in load-sharing and failure mechanisms of the spine under different loading conditions.

Keywords Bone fracture · Dynamic load · Finite element model · Ligament tear · Lumbar spine · Experimental validation

E. Wagnac · A. Garo · C.-E. Aubin (✉)
Biomedical Engineering Institute, École Polytechnique
de Montréal, P.O. Box 6079, Station Centre-Ville, Montréal,
QC H3C 3A7, Canada
e-mail: carl-eric.aubin@polymtl.ca

E. Wagnac · P.-J. Arnoux · A. Garo
Laboratoire de Biomécanique Appliquée, IFSTTAR-Aix-
Marseille University, Faculté de Médecine secteur Nord,
Boulevard Pierre Dramard, 13916 Marseille Cedex 20, France

C.-E. Aubin
Research Center, Sainte-Justine University Hospital Center,
3175 Côte Sainte-Catherine Rd, Montréal, QC H3T 1C5, Canada

1 Introduction

Lumbar spine injuries, such as vertebral fractures and ligament tears, are significant causes of disability for healthy individuals, thus inducing high socioeconomic consequences [37]. Multi-directional dynamic loading mechanisms sustained during traumatic events, such as falls and motor vehicle crashes, are recognized as the primary causes of spinal injuries [10, 12, 21].

It is well known that the rate at which dynamic loads are applied will modulate the mechanical response of individual tissues [14, 25, 30]. However, the effect of the loading or displacement rate (which is easier to control experimentally, especially at high rates) on lumbar spine injuries remains unclear. Results from experimental studies provide some insight, but, mostly, these studies have been performed on short spinal segments and tested for a single load direction [1, 24, 38, 45, 46]. Moreover, the biological variations of the specimens as well as the non-systematic measurement of many parameters impaired the possibility to compare results, thus questioning the ability of experimental studies to provide an exhaustive evaluation of the influence of load/displacement rate on the failure mechanisms of the spine.

Currently, numerical human models based on a finite element (FE) formulation are widely used for injury biomechanics research [44], as they obviate the need for

experimental work. Within the field of finite element analysis (FEA) studies, much work has been done on human models dedicated to the virtual assessment of trauma on different body parts [11]. Research on the bio-mechanics of lumbar spine injury and response is not as advanced as research on body regions that are more frequently injured, such as the cervical spine, head, or thorax [18]. For example, FEA of models of the normal lumbar spine, developed in isolation [29, 43] or as part of complete human body models [11, 44], do not present the ability to thoroughly investigate the influence of the load/displacement rate on lumbar spine injuries. This situation is a consequence of limitations of the models in terms of geometry (e.g., ligaments not included), material constitutive law (e.g., material laws without strain/load rate dependency and with properties calibrated using experimental data obtained quasi-statically), or loading (e.g., use of single load direction).

To overcome these simplifications, an anatomically realistic and detailed three-dimensional solid finite element model (FEM) of L2–L3 was developed jointly by Polytechnique Montreal and the Laboratory of Biomechanics and Applications of IFSTTAR/Aix-Marseille University [6, 39]. The model, named Spine Model for Safety and Surgery (SM2S), was built for both quasi-static (implant biomechanics) [39] and dynamic (virtual trauma analysis, design of safety devices) [6] applications. Recently, the model was used to demonstrate the influence of rotation rate on the load-sharing mechanisms and the onset of spinal injuries amongst vertebral structures in flexion/extension [6]. To more closely reflect real-life trauma situations,

which involve multi-directional loading applied to complete lumbar spine segments [22], the SM2S model should be extended to the full lumbar spine segment and revised to incorporate validated multi-directional biomechanical behavior at different displacement rates.

Accordingly, the purposes of the present study were (1) to present the development and validation of the full lumbar spine SM2S (T12–L5) subjected to low and high dynamic compression, flexion, extension, anterior shear, and posterior shear and (2) to utilize this validated model to investigate the influence of displacement rate on spinal injuries, under these loading conditions.

2 Materials and methods

2.1 Geometric modeling and meshing

The detailed solid model of the full lumbar spine (Fig. 1) was derived from the L2–L3 model presented by El-Rich et al. [6]. Thus, the bony geometry of the T12–L5 model was reconstructed from CT-scan images (contiguous slices of 0.6 mm thick) of a 50th percentile healthy male volunteer (Caucasian, 32 years old, ~75.5 kg, ~1.75 m) without spine pathology. To reference the model, the x, y, and z axis were set in the ventral, cranial, and right lateral directions, respectively. The resulting surface of each vertebra was freely meshed using three-node shell elements, which were subdivided into nine areas of different thicknesses [7, 31] that either belong to cortical bone or vertebral endplates (Fig. 2a). Shell elements were filled

Fig. 1 Finite element model of the T12–L5 segment of the Spine Model for Safety and Surgery (SM2S). The model was composed of the T12 (1) to L5 (2) vertebrae, the intervertebral discs (3), each divided into the nucleus (4), annulus (5) and collagen fibers (6), and the anterior longitudinal (ALL, 7) the posterior longitudinal (PLL, 8), the capsular (CL, 9), the flavum (FL, 10), intertransverse (ITL, 11), supraspinous (SSL, 12), and interspinous (ISL, 13) ligaments
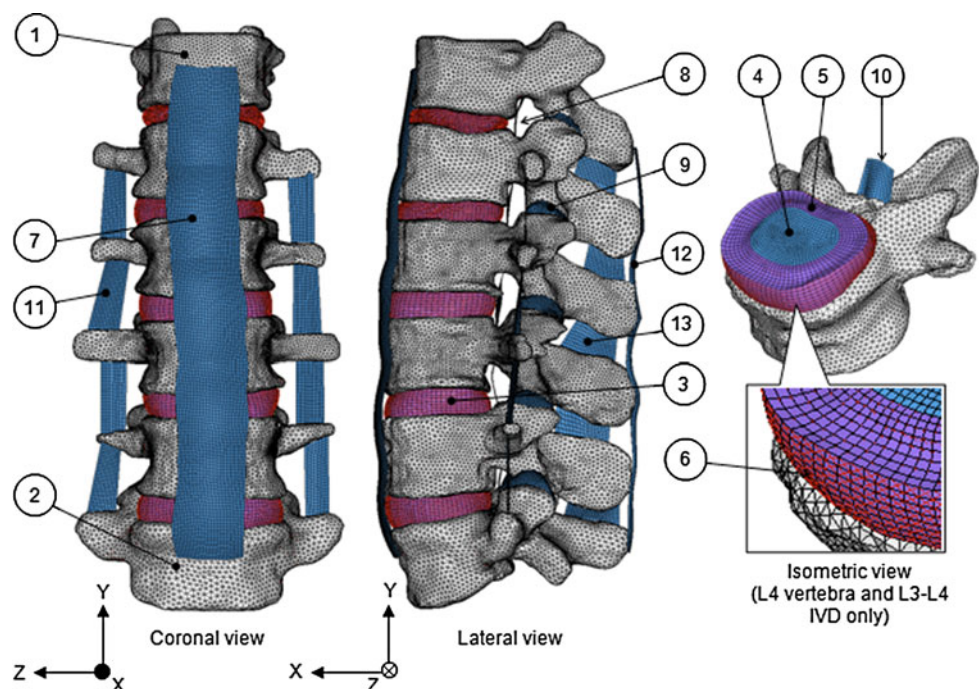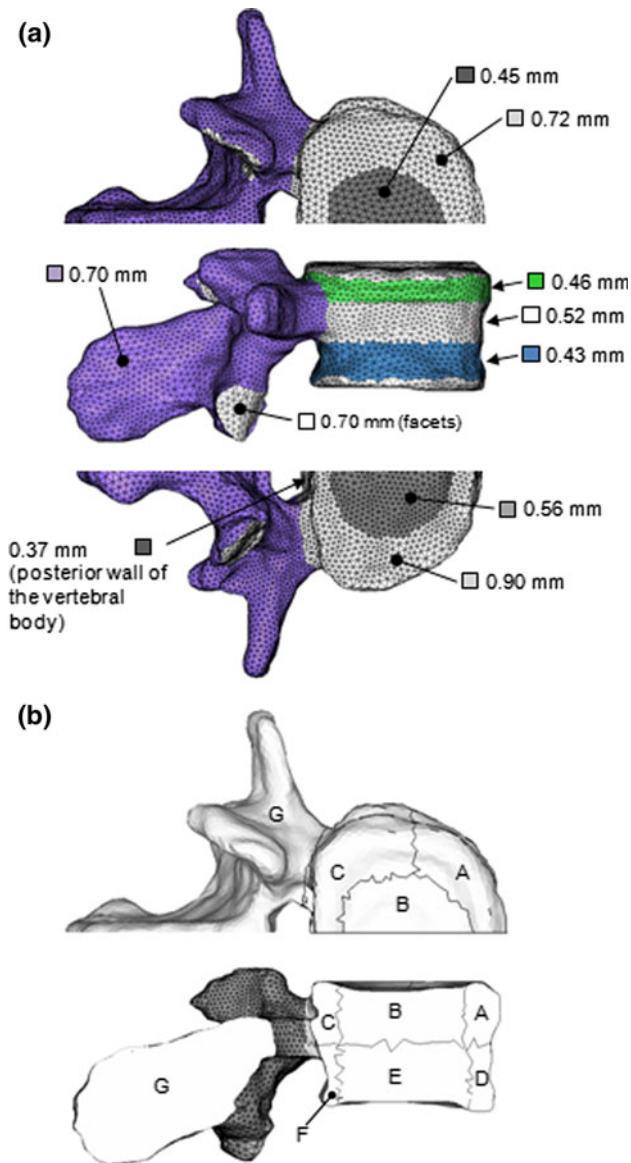
Fig. 2 a Subdivision of the vertebrae into nine zones of different cortical bone thicknesses (e.g. L3). **b** Subdivision of the cancellous bone into seven zones of different material properties (e.g. L3)

with four-node solid elements, which were, in turn, divided into seven zones (A–G, Fig. 2b), each with a different combination of architecture and mineral density for the cancellous bone [47].

The geometry of each intervertebral disc (IVD) was created between the intervening vertebral endplates and subdivided into the nucleus pulposus and the annulus fibrosus (volume ratio $\approx 56\%$ annulus and 44 % nucleus) based on published anatomical data [17, 42]. Each IVD was modeled by eight layers of eight-node solid elements. In the annulus fibrosus, the ground substance was reinforced by collagenous fibers, which were modeled by tension-only spring elements organized in concentric lamellae with a crosswise pattern at an orientation of $\pm 35°$ [33].

Surface models of the anterior longitudinal (ALL), posterior longitudinal (PLL), capsular (CL), flavum (FL), intertransverse (ITL), supraspinous (SSL), and interspinous (ISL) ligaments were created between each spinal motion segment based on literature, dissection results, and histological findings [28]. The ligaments were meshed with three-node (CL only) and four-node shell elements. In total, the mesh of the T12–L5 model contained 105,000 nodes and 447,000 elements, with characteristic length varying from 1.0 to 2.5 mm. The final sizes of the components (vertebral bodies, IVDs, and ligaments) were selected through convergence studies, which ensured that the chosen mesh resolutions were not significantly less accurate than finer mesh resolutions. This ensured a satisfactory balance between accuracy and computing time/cost.

2.2 Material constitutive laws

These were based on those utilized in the FEA study on the L2–L3 model [6]. Bony components were assumed as isotropic materials and followed a symmetric and strain rate-dependent elasto-plastic (Johnson–Cook) material law (Table 1). Prior to the onset of plasticity (equivalent stress < yield stress), each of these materials was assume to behave as a linear elastic solid. During plastic deformation, the equivalent stress at constant temperature was described with the relation:

$$\sigma = \left(a + b\varepsilon_p^n\right) * \left(1 + \ln\left(\frac{\dot{\varepsilon}}{\dot{\varepsilon}_0}\right)\right),$$

where σ equivalent stress, a yield stress, b hardening modulus, n hardening exponent, ε_p plastic strain (true strain), $\dot{\varepsilon}$ current strain rate, and $\dot{\varepsilon}_0$ reference strain rate.

Once the ultimate deformation level (ε_{MAX}) is reached, failure is modeled without any damage effect using a kill element model [6, 8, 9].

The fluid-like behavior of the nucleus pulposus and the properties of the ground substance of the annulus fibrosus were each modeled using a hyperelastic material law based on a first-order Mooney–Rivlin formulation, described by the following formulation for the strain energy function, W:

$$W = C_{10}(I_1 - 3) + C_{01}(I_2 - 3) + \frac{(J - 1)^2}{d},$$

where C_{10}, C_{01} material constants; I_1, I_2 first and second invariants of the deviatoric components of the left Cauchy-Green strain tensor; J local volume ratio; d $2/K$;

$$K = 6(C_{10} + C_{01})/3(1 - 2v).$$

Two sets of material properties were defined by using the calibration method proposed by Wagnac et al. [41]

Table 1 Mechanical properties of bony tissues in the model (adapted from [9])

Material properties	Cancellous bone (per zone) and bony endplate center[a]							Cortical bone and bony endplate margin
	A	B	C	D	E	F	G	
Density ($\times 10^{-3}$ g/mm^3)	1.8	1.8	2.0	2.0	2.5	2.5	1.8	0.2
Modulus of elasticity, E (MPa)	93.7	93.7	93.7	93.7	93.7	93.7	93.7	4,014
Poisson's ratio, v	0.25	0.25	0.25	0.25	0.25	0.25	0.25	0.3
Yield stress, a (MPa)	1.95	1.95	1.95	1.95	1.95	1.95	1.95	105
Hardening modulus, b (MPa)	8.5	7.0	8.5	8.1	12.5	12.5	7.0	492.9
Hardening exponent, n	1	1	1	1	1	1	1	1
Failure plastic strain, ε_p	0.082	0.06	0.082	0.08	0.104	0.104	0.06	0.071
Maximum stress (MPa)	2.65	2.3	2.65	2.6	3.25	3.25	2.3	140
Strain rate coefficient, c	0.533	0.533	0.533	0.533	0.533	0.533	0.533	0.272
Reference strain rate, $\dot{\varepsilon}_0$	0.008	0.008	0.008	0.008	0.008	0.008	0.008	0.008

[a] Material properties used for the bony endplate center are the same as zone B

since the Mooney–Rivlin hyperelastic material law does not incorporate strain rate dependency into its formulation. One set was calibrated at a low dynamic compression rate of 0.1 m/s while the other set was calibrated at a higher dynamic compression rate of 1 m/s (Table 2a). The fibers of the annulus fibrosus were modeled using a non-linear load–displacement curve [41] adapted from literature results [36].

The ligaments were governed by a non-linear strain rate-dependant material formulation [6]. Ligament damage and failure were implemented through a failure model based on tensile principal strain criterion. Ligament properties were calibrated using experimental data measured at different load rates [40]. The values are provided in Table 2b.

Tied interfaces (kinematic conditions) were used between soft tissues (IVDs and ligaments) and bony components in order to prevent any relative movement. Frictionless contact interfaces, to avoid penetration between adjacent components of the model [1], were assumed between articular facets.

Table 2 Mechanical properties of the soft tissues (a) intervertebral discs, (b) spinal ligaments

Material properties	Nucleus pulposus		Annulus matrix		Fibers	Ref.
	Low dyn.	High dyn.	Low dyn.	High dyn.		
a.						
Density (E^{-6} kg/mm^3)	1	1	1.2	1.2	–	[41]
Poisson's ratio, v	0.499	0.499	0.45	0.45	–	[41]
C_{10}	0.64	31.8	0.24	11.8	–	[41]
C_{01}	−0.16	−8.0	−0.06	−2.9	–	[41]
Load–disp. curve	–	–	–	–	Nonlinear	[36]

Material properties	Spinal ligaments							Ref.
	ALL	PLL	CL	LF	ISL	SSL	ITL	
b.								
Density (E^{-6} kg/mm^3)	1	1	1	1	1	1	1	[6]
Modulus of elasticity E (MPa)	19.2	84.1	0.6	4.2	4.7	10.2	4.7	[40]
Poisson's ratio, v	0.4	0.4	0.4	0.4	0.4	0.4	0.4	[40]
Update coef., E_1 (MPa/ms)	469.4	1,432.1	3.6	199.7	98.3	476.5	98.3	[40]
Update coef., E_2 (MPa)	19.0	83.5	0.6	4.0	4.6	10.0	4.6	[40]
Failure strain, ε_1	0.68	0.38	1.75	1.01	1.10	0.94	1.10	[40]
Failure strain, ε_2	0.90	0.50	1.85	1.25	1.30	1.08	1.30	[40]
Scaling function, SF	Tabulated curves							[40]

2.3 Model validation under dynamic loading conditions

An extensive multi-directional validation of the T12–L5 spinal segment of SM2S was performed against published experimental data measured under low (LD) and high dynamic (HD) loading conditions [2, 3, 5]. Up to five modes of loading were used for the validation depending on the availability of experimental data. Validation of LD loading conditions was performed in compression, flexion (forward bending), extension (backward bending), anterior shear, and posterior shear. Validation of HD loading conditions was performed in compression, flexion, and extension.

To mimic the experimental setup, the proximal vertebra (T12) and the distal vertebra (L5) of the SM2S model were set as rigid bodies. Masses (1.6 kg) were added to these bodies in order to simulate the fixture used during the experiments [2]. In all the simulations, L5 was fully constrained in all degrees of freedom. Specific boundary and loading conditions were applied to the rigid body of the proximal vertebra (T12) in the form of imposed displacement rate (or velocity) vectors (V_X, V_Y, or V_Z) according to the simulation performed (Table 3). The displacement rates applied to L5 were based on the experiments. Consequently, all simulations under LD conditions were run at a displacement rate of 0.1 m/s [3] while simulations under HD loading conditions were run at a displacement rates of 1 m/s (compression [5]) and 4 m/s (flexion and extension [2]). At the beginning of each simulation, the T12–L5 spinal segment was unloaded and had a lordotic angle of 25°. This lordotic angle was similar to the natural lordotic angle of the unloaded spinal specimens measured before the experimental tests [2, 3, 5].

Force (F)–displacement (D) curves were extracted from axial and shear loading simulations, while moment (M)–angular rotation (R) curves were extracted from bending simulations. The moment (M)–displacement (D) curve of the HD compression simulation was also extracted since it was available experimentally. The stiffness (K) and the maximum load were extracted from each curve and compared to experimental values. K was calculated by linear regression of the final portion of the curves [2, 3]. The maximum load was defined in accordance with the experiments:

- In HD compression, the maximum load was the load observed at the point of failure (F_{FAIL}) [5]. The point of failure was defined as the point at which a further increase in displacement/rotation resulted in a decrease in external force/moment.
- In HD flexion and extension, the maximum load (M_{MAX}) was the maximum bending moment reached after a displacement of 38.1 mm, as prescribed experimentally [2].
- In LD conditions, the maximum load (F_{MAX} or M_{MAX}) was the force reached at the displacement prescribed experimentally (compression 6.35 mm, flexion and extension 50.8 mm, and lateral bending, anterior shear and posterior shear 38.1 mm) [3].

Displacements prescribed experimentally were set before any sign of failure of the specimens were observed ($F_{MAX} < F_{FAIL}$; $M_{MAX} < M_{FAIL}$). Consequently, the failure loads (F_{FAIL} or M_{FAIL}) for all LD and HD simulations (except HD compression) were not compared to experimental results.

All the simulations were performed using an explicit dynamic solver that includes non-linear large deformations (Radioss version 10.0, Altair Engineering inc., Troy, MI, USA).

2.4 Comparison of failure behavior of T12–L5 under dynamic loading conditions

The SM2S model was used to compare the spinal injuries predicted when submitted to compression, flexion, extension, anterior shear, and posterior shear at low and high displacement rates. Simulation parameters were the same as those reported for the validation, except that all

Table 3 Summary of the 8 simulations performed for the validation of the T12–L5 segment of SM2S under low dynamic (LD) and high dynamic (HD) loading conditions

Load case	Case #	Type of loading	Free DOF on T12	Applied loads on T12	Experimental results for validation
Compression	1	LD	T_Y	$V_Y = -0.1$ m/s	F–D curves, K, F_{MAX}
	2	HD	T_Y	$V_Y = -1.0$ m/s	F–D curves, K, F_{FAIL}
Flexion	3	LD	ALL	$V_X = +0.1$ m/s	M–A curves, K, M_{MAX}
	4	HD	ALL	$V_X = +4.0$ m/s	M–A curves, K, M_{MAX}
Extension	5	LD	ALL	$V_X = -0.1$ m/s	M–A curves, K, M_{MAX}
	6	HD	ALL	$V_X = -4.0$ m/s	M–A curves, K, M_{MAX}
Anterior shear	7	LD	T_X	$V_X = +0.1$ m/s	F–D curves, K, F_{MAX}
Posterior shear	8	LD	T_X	$V_X = -0.1$ m/s	F–D curves, K, F_{MAX}

simulations were run up to failure. Displacement rates of 4 m/s were used for the HD anterior shear and posterior shear simulations. Results extracted for comparison included the initiation sites of spinal injuries (bone fracture and/ or ligament rupture), the load at failure (F_{FAIL} and M_{FAIL}), the displacement (D_{FAIL}), or angular rotation (θ_{FAIL}) at failure, the contact forces in the articular facets (FF_{FAIL}), the intradiscal pressure in the nucleus at failure (IDP_{FAIL}), and the maximum von Mises stress in the annulus (VM_{FAIL}). FF_{FAIL} was computed by the vectorial summation of forces at various contact regions on the two facets of

each spinal level [35]. IDP_{FAIL} was computed as one-third of the trace of the stress tensor since the nucleus was generated with solid elements [33].

3 Results

3.1 Validation of the model

The simulations performed under LD conditions (0.1 m/s) resulted in non-linear F–D and M–R curves (Fig. 3). With

Fig. 3 Simulated force–displacement and moment–angular rotation curves versus experimental corridors under low dynamic (LD) conditions. **a** Compression, **b** flexion, **c** extension, **d** anterior shear, and **e** posterior shear
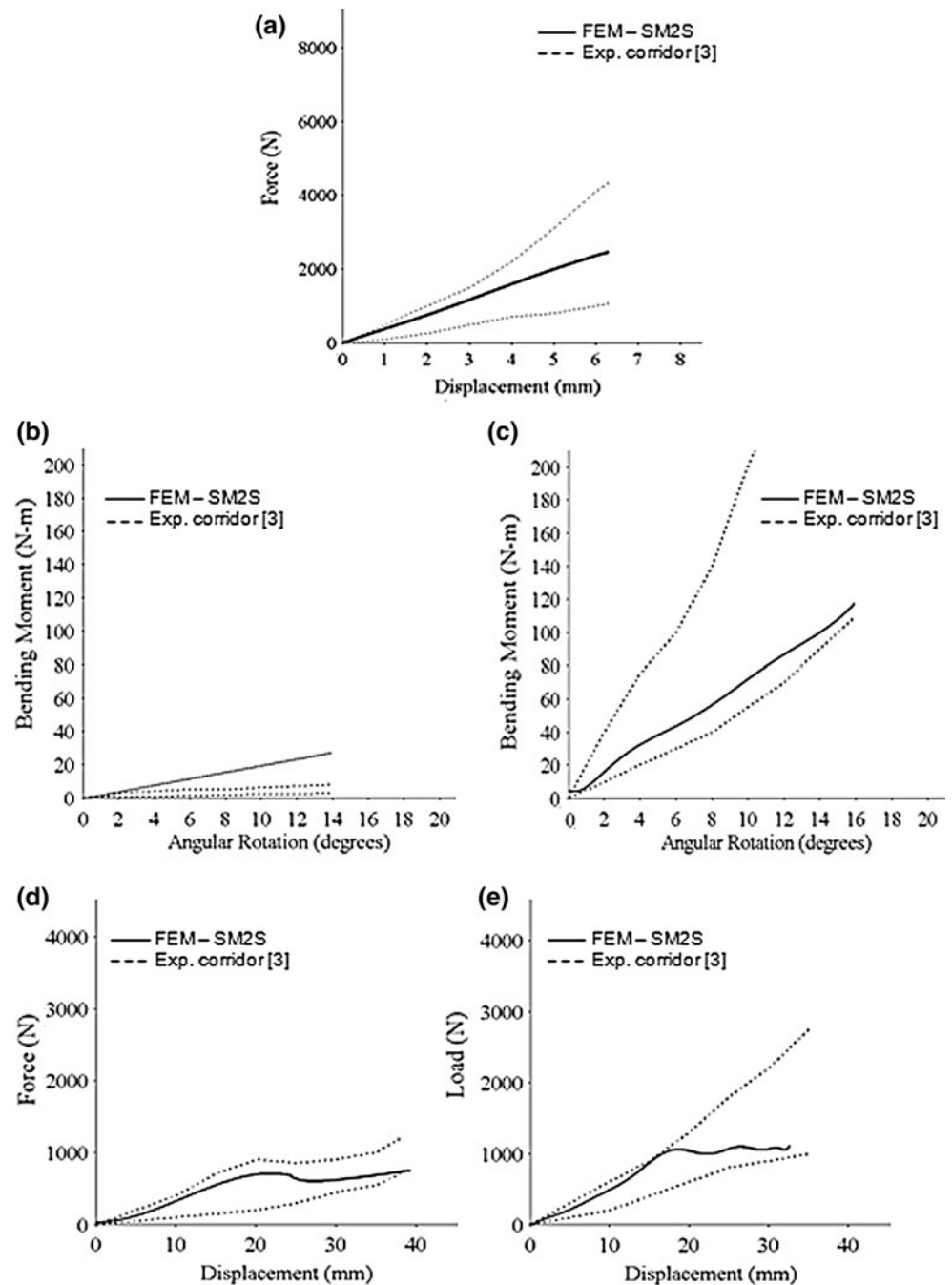
one exception, each of these curves and the derived parameters fell within the experimental corridors (Table 4). The exception was that, in flexion, K and M_{MAX} were higher than the maximum experimental values.

The simulated F–D and M–D curves obtained in HD compression (1 m/s) showed values for K and failure parameters that were similar to the corresponding experimental results obtained under similar conditions [5] (Fig. 4). In HD flexion and extension (4 m/s), M_{MAX} and the corresponding resulting forces (vertical and horizontal) were lower (by <15 %) than the minimum experimentally obtained values (Table 5).

3.2 Comparison of failure behavior of the model under dynamic loading conditions

At failure, there were higher forces and moments for simulations under HD loading conditions than under LD ones (Fig. 5). Also, the HD simulations showed lower displacements and angular rotations at failure than simulations under LD loading conditions.

Different initiation sites were observed for spinal injuries produced in LD and HD compression, flexion, and extension. In LD compression, a bone fracture was initiated at the center of the endplate of L1 (Fig. 6a) while, in HD compression, it was initiated in the upper part of the vertebral body of L1 (Fig. 6b).

In LD flexion, ligament rupture and bone fracture were initiated in the L4–L5 ISL and CL ligaments and in the posterior rim of the L4 inferior endplate, respectively (Fig. 6c). The rupture of the L4–L5 ISL ligament was also observed in HD flexion, but the bone fracture was initiated in the anterior part of the L4 vertebra (Fig. 6d). In LD extension, fractures were initiated in the spinous process of the L3 and L5 vertebrae (Fig. 6e), while in HD extension, fractures were initiated in the anterior rim of the L4 inferior endplate (Fig. 6f).

Table 4 Validation results under low dynamic (LD) compression, flexion, extension, anterior shear, and posterior shear

Load case	K (N/mm or N-m/°)		F_{MAX} (N)		M_{MAX} (N-m)	
	SM2S	EXP	SM2S	EXP	SM2S	EXP
Compression	386	520 ± 284	2,484	$2,350 \pm 1,210$	–	–
Flexion	2.0[a]	0.6 ± 0.4[a]	–	–	30.9	7.0 ± 3.0
Extension	9.2[a]	16.4 ± 7.1[a]	–	–	118	182 ± 92
Anterior shear	41	38 ± 10	708	830 ± 170	–	–
Posterior shear	87	70 ± 16	1,060	$1,760 \pm 570$	–	–

[a] Units are in N-m/°

Fig. 4 Simulated versus experimental test results under high dynamic (HD) compression. **a** Force–displacement curves and **b** moment–displacement curves
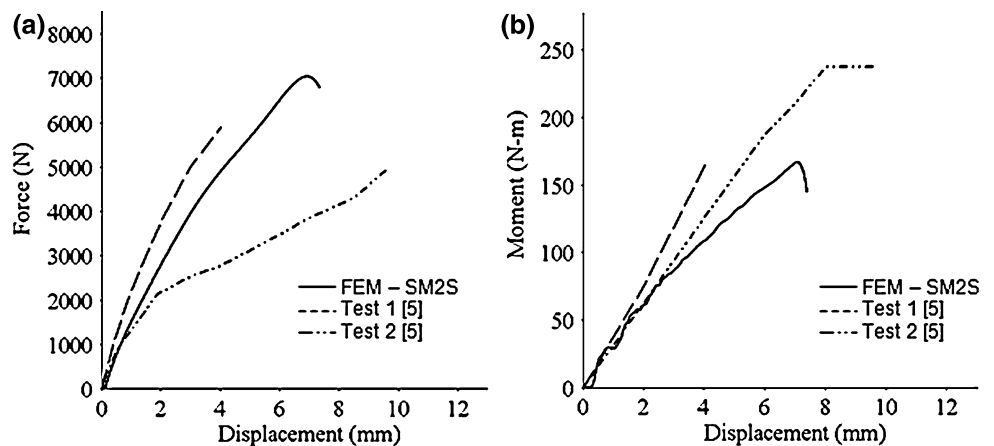

Table 5 Validation results under high dynamic (HD) flexion and extension

[a] Maximum values reached after a linear displacement of 38.1 mm

Results	Flexion		Extension	
	FEM	EXP	FEM	EXP
M_{Z-MAX} (N-m)[a]	105	164 ± 43	146	201 ± 48
F_{XY-MAX} (N)[a]	733	$1,196 \pm 261$	856	$1,181 \pm 252$

Fig. 5 Simulated force–displacement and moment–angular rotation curves in LD and HD loading conditions. **a** Compression, **b** flexion, **c** extension, **d** anterior shear, and **e** posterior shear
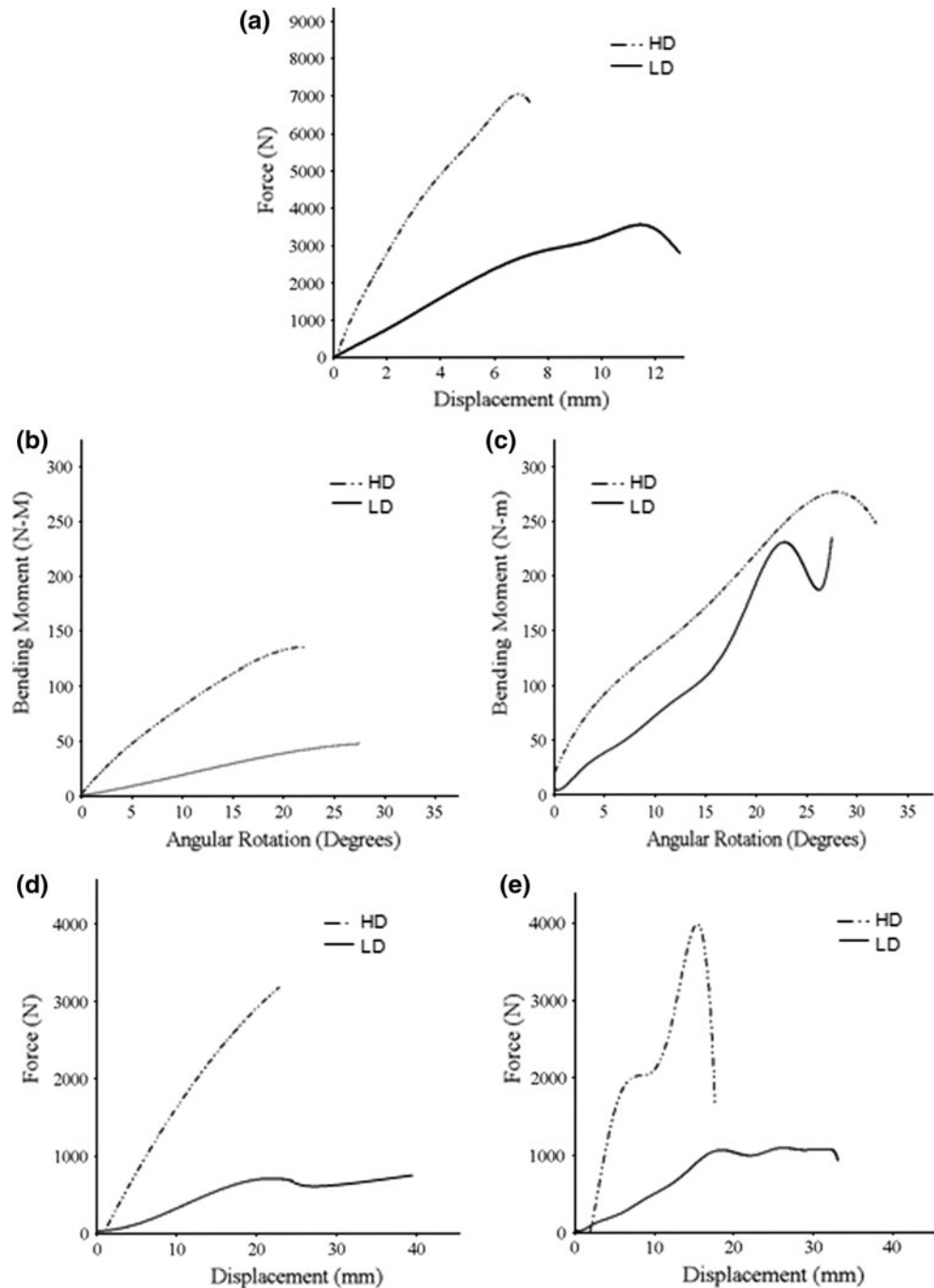
Similar initiation sites were observed under LD and HD shear loading conditions. Indeed, a rupture of the L4–L5 ISL and CL ligaments, a fracture of the anterior rim of the L1 superior endplate, and a fracture of the posterior rim of the L4 inferior endplate were initiated in both LD and HD anterior shear (Fig. 6g). A fracture was also initiated in the pars interarticularis of L1 (not shown). In both LD and HD posterior shear, fractures were initiated in the anterior rim of the L4 inferior endplate (Fig. 6h, i) and under the L4 spinous process (not shown). Under LD conditions, however, a second

fracture was initiated in the posterior rim of the L1 superior endplate (Fig. 6h). Under HD conditions, this second fracture was initiated in the posterior elements of L1, underneath the T12–L1 LF ligament (Fig. 6i).

Prior to failure, different IDP distributions were observed between spinal levels under LD and HD compression (Fig. 7a). In LD compression, the highest IDP was observed at the T12–L1 level while it was at the L4–L5 level under HD compression. The IDP distributions between LD and HD loading conditions were similar for all

other modes of loading. Indeed, in LD and HD flexion and extension, the IDP increased caudally (Fig. 7b, c). In LD and HD anterior shear, low IDP was obtained for all levels, except at L4–L5 (Fig. 7d). Little or no IDP was observed in mid-levels of the lumbar spine (from L1–L2 to L3–L4) under both LD and HD posterior shear (Fig. 7e). For all loading modes, IDP values were higher under LD loading conditions compared to HD ones.

In each of the loading cases, simulations under HD loading conditions generated higher Von Mises stresses in the annulus than under LD conditions. Stress distributions (annulus with the higher peak stress) across levels were, however, the same under both dynamic loading conditions. In compression, peak stresses were mostly located in the posterior part of the annulus and increased cranially between levels (from L4–L5 to T12–L1) (Fig. 7a). In

Fig. 6 Initiation sites of spinal injuries according to the loading mode. **a** LD compression, **b** HD compression, **c** LD flexion, **d** HD flexion, **e** LD extension, **f** HD extension, **g** LD and HD anterior shear, **h** LD posterior shear, and **i** HD posterior shear
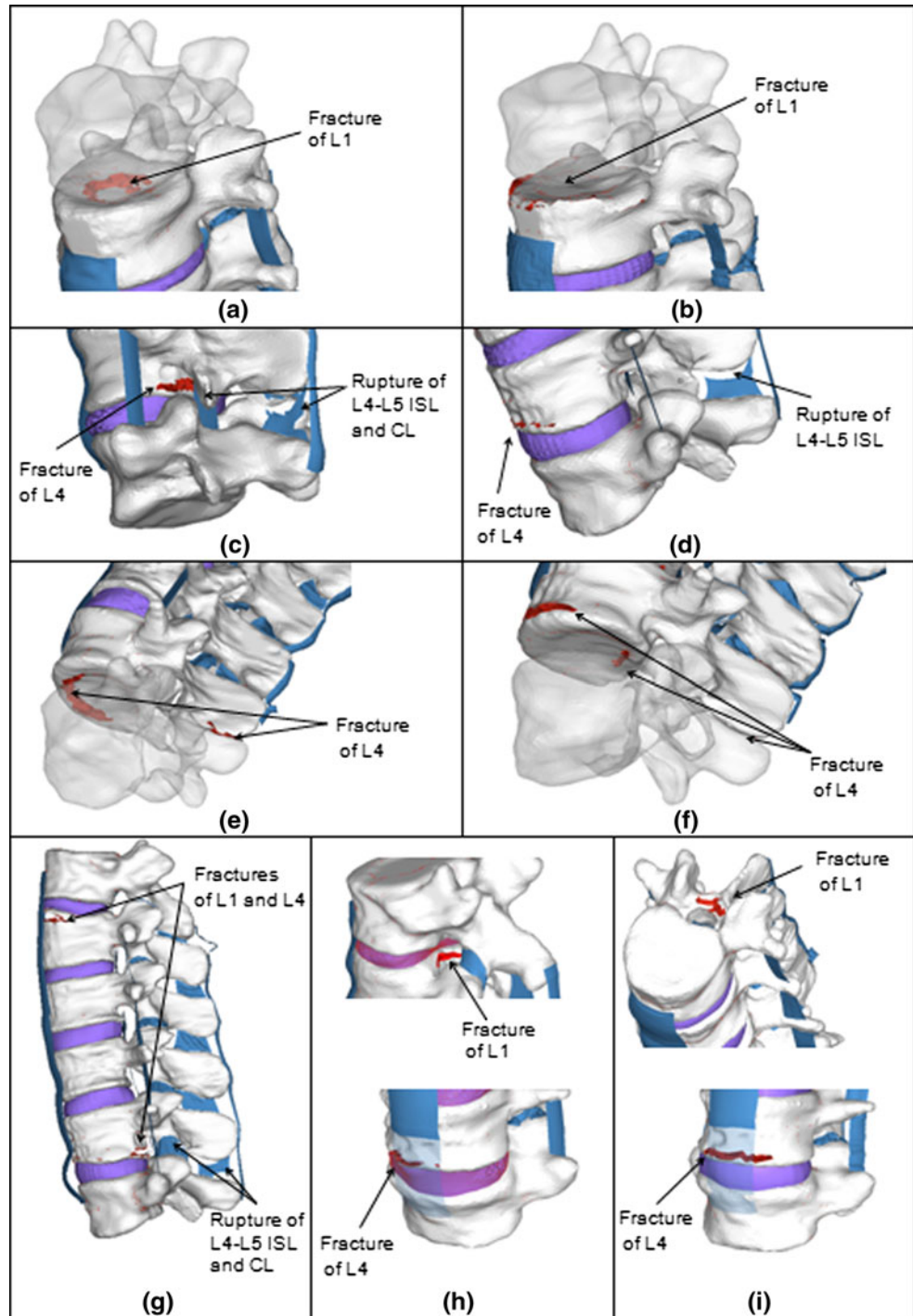
Fig. 7 Intradiscal pressures, maximum von Mises stresses in the annulus, and total contact forces in the facets at initiation of failure, under LD and HD loading conditions.
a Compression, **b** flexion, **c** extension, **d** anterior shear, and **e** posterior shear
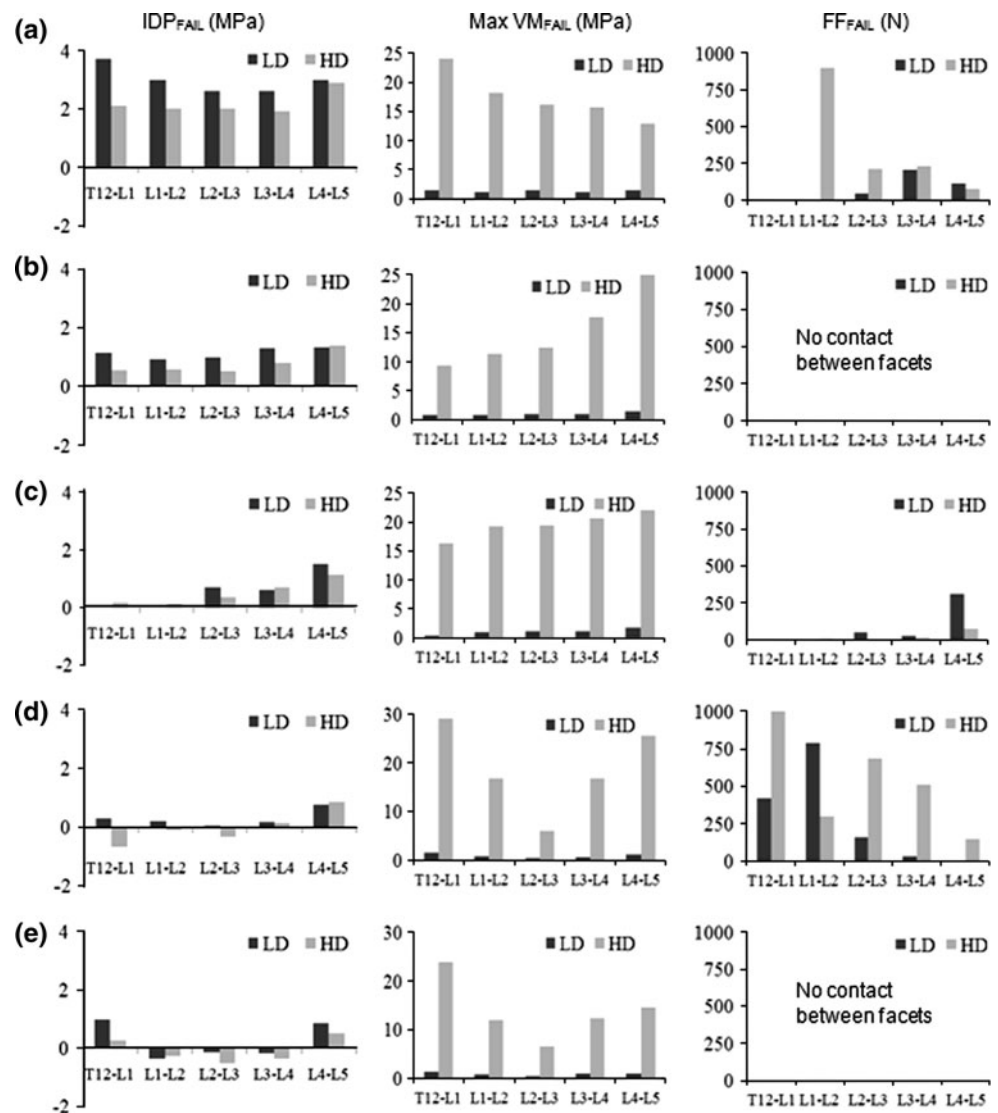
flexion and extension, peak stresses were, respectively, located in the anterior and posterior part of the annulus. In both cases, peak stresses increased caudally between levels (Fig. 7b, c). In anterior and posterior shear, peak stress location within the annulus (anterior or posterior) varied across levels. Peak stresses were higher at both extremities of the lumbar spine (T12–L1 and L4–L5) (Fig. 7d, e).

No contact forces were observed under LD and HD flexion and posterior shear. Under each of these conditions, capsular ligaments were stretched to provide resistance to motion.

In compression, high facet forces were generated under HD loading conditions, especially at the L1–L2 level, while lower facet forces were generated under LD loading conditions. Very low facet forces were observed under both LD and HD extension. In compression and extension, contact forces were generated between the spinous process of the L4 and L5 vertebrae. This interaction between

spinous processes was also detected under posterior shear. Finally, high facet forces were observed under both LD and HD anterior shear.

4 Discussion

In the present study, a three-dimensional solid model of a normal T12–L5 spine segment was developed for FEA study of spinal injuries. This numerical model distinguishes itself from other published models [11, 13, 19, 29, 43, 44] by utilizing a detailed solid model, a fine FE mesh, and strain-dependant material constitutive laws that simulate bone fracture and ligament tear. These model improvements allowed precise simulation of the biomechanical behavior of the spinal components up to failure, under low (0.1 m/s), and high (1 m/s and 4 m/s) displacement rates, which represent greater displacement rates than used in

most previous studies (the rates used in these studies are low enough for the loading to be considered quasi-static).

Under LD loading conditions, the gross biomechanical behavior of the model in the sagittal plane, as described by the load–displacement curves (Fig. 3), was in good agreement with the experimentally determined in vitro data. The simulated maximum loads in HD compression, flexion and extension were either within or very close to the experimental corridors (Fig. 4; Table 5). However, the first loading phase observed experimentally in HD flexion and extension [2] was not reproduced. This phase was characterized by a large initial rotation of the free end of the specimen in the direction of the loading without a notable increase in moment, immediately followed by a moment in the opposite direction. Only the phase characterized by an increasing moment in the direction of loading was simulated.

The discrepancies observed between the FEM and the cadaveric specimens (e.g., in LD and HD flexion, and HD extension) can, mostly, be attributed to the fact that material properties used to simulate the bone and IVD components were isotropic, symmetric, and calibrated in compression. The multi-directional calibration method proposed by Schmidt et al. [32] for the IVD could have been used, but such a method requires a large number of experiments which are not yet available. Discrepancies may also be attributed to the fact that the so-called initial "toe region" (where an increase in length is observed without a significant force increase) of the spinal ligaments was not implemented into the FEM, thus overestimating ligament stiffness in the neutral zone. Discrepancies may also be attributed to the absence of articular cartilage and synovial fluid at the facet joints, which may underestimate the load shared by the facets especially under compression, extension, anterior shear and posterior shear. Other limitations may be defined by differences between the experimental setup (age of the specimens, loading/boundary conditions, etc.) and the FEM. Such inherent limitations may have contributed to discrepancies, and this should be considered when interpreting the results.

Because of the paucity of in vitro data characterizing the biomechanical behavior of the spine under dynamic loading conditions up to failure, it was not possible to directly validate the stress and strain fields and contact forces throughout the spinal segment, nor the initiation sites of spinal injuries. Since these data are not easily amenable via direct experimental measurements, the evaluation provided in the present study represents a first but significant step towards the development of a FEA of models of spine segments under loading conditions experienced in trauma situations. Obviously, under in vivo conditions, complex combined loads are usually involved so that comparison of the spinal injuries predicted in the current study under simple loads, without muscular, intra-abdominal pressure, and gravity effects, with those observed clinically should be performed with care. This last statement is further emphasized by the fact that spinal injuries were modeled through an element deletion process that accurately predicts the initiation site of an injury (bone fracture or ligament rupture), but not its final state, as observed by clinicians after trauma.

The comparison between the biomechanical behavior of the lumbar spine under LD and HD conditions further demonstrates the ability of the FEM to virtually assess spinal injuries under different loading rates. Indeed, under HD loading conditions, the model displayed higher stiffness and loads to failure, but lower displacements (linear and angular) to failure, which is consistent with experimental observations in axial compression [16, 45], anterior shear [46], and flexion-shear loads [23, 24, 27]. By modulating the load-sharing mechanism amongst the different spinal components in response to the different loading rates, the model was also able to predict the onset of spinal injuries for a given loading direction.

Also, the comparative analysis provided new insight into the biomechanics of spinal injuries. For instance, the large stress sustained by the annulus under HD loading conditions, as opposed to the nucleus, suggests that the annulus bears a higher portion of the load in HD loading conditions. As a matter of fact, bone fractures were all located in the vertebra adjacent to the IVD with the highest peak von Mises stress.

Simulations in LD and HD compression confirmed that in healthy IVDs, bone fractures are initiated in the middle of the endplate and in the cancellous bone under the nucleus, as observed by Shirado et al. [34]. Accordingly, the endplate and vertebral body fractures observed in LD and HD compression are in agreement with the findings of Yingling et al. [45]. The fact that the intradiscal pressure at failure was slightly higher under LD loading conditions than under HD loading conditions suggests that the sudden penetration of the nucleus material through the endplate of the vertebra might not be the sole cause of severe compression fractures (e.g., burst fractures). Facet joints could also play a crucial role, as hypothesized by Langrana et al. [20] and Wilcox et al. [43], by transmitting shear forces to the posterior upper half of the vertebral body. In the present study, the higher facet loads observed in HD compression at the L1–L2 level resulted in higher stress concentrations at the base of the pedicle, thus supporting this hypothesis.

In LD flexion, the low stiffness of the annulus allows the anterior part of the disc to compress, bulge, and, with the combined action of the posterior ligaments, generate tensile stress and strain in the postero-inferior part of the vertebral bodies. The rupture of the ISL at the L4–L5 level under both LD and HD loading conditions further suggests

that when an anterior wedge fracture or an endplate avulsion of the posterior rim is diagnosed, the posterior ligamentous complex might be at risk for ligament injury.

The IVD material properties also played a significant role in extension. Indeed, the low stiffness of the annulus and the nucleus, under LD conditions, offered little resistance to the extension moment. This resistance was mostly provided by the spinous process of the L3, L4, and L5 vertebrae that failed shortly after contact. Such spinous process fractures are very uncommon and should be attributed to the small initial distance between the adjacent spinous processes and the low facet forces generated by the model. In fact, these low forces observed in both LD and HD extensions were unexpected since facet articulations generally play a significant role in extension [35]. The movement patterns, the specific facet geometries and modeling limitations (no articular cartilage and synovial fluid), and the absence of combined axial compression (or preload) are factors that could explain this limited role. This type of hyperextension injury is usually seen in pilots after ejection from military aircraft [15].

The biomechanical observations made in flexion and extension can be directly applied to the case of pure shear loads. For instance, LD and HD anterior shear puts the T12–L1 motion segment in extension and the L4–L5 motion in flexion, while the opposite is observed in posterior shear. Consequently, spinal injuries observed in anterior and posterior shear loads were similar to those reported in flexion and extension. The anterior translation movement of the T12 vertebra also induces large facet loads at the T12–L1 level and causes fractures of the pars interarticularis of L1. Similar types of fractures were observed by Yingling et al. [46] after exposing porcine cervical motion segments to anterior shear loads under quasi-static and dynamic loading conditions.

In the present work, a detailed FEA of a model of the full lumbar spine dedicated to the virtual assessment of bone and ligament injuries in multiple loading conditions was presented and validated. The proposed lumbar spine model takes into account the rate-dependency and failure behavior of spinal components. However, the model did not consider the active and passive muscular responses, which might alter the lumbar spine kinematics and load-sharing amongst components during the interval in which injury likely occurs. But whether muscular reaction mitigates or exacerbates spinal injuries remains unclear and the complex loads sustained by the spine during real-life trauma situations need to be precisely quantified. Also, the model did not take into account the fluid flow that occurs between spinal components in response to loading, and which could be achieved by using poroelastic material laws. The assumption of no fluid flow in the spinal components was appropriate here since the study was focused on the mechanical response of the lumbar spine to dynamic loading velocities, as opposed to long-term gravitational loads, which may induce a visco-poroelastic response over a timeframe of minutes or hours. Indeed, it is accepted that the fluid within the cartilage matrix and the vertebrae has a limited flow under high strain rates or high velocities [26] and that for such loading conditions, the cartilage response relies on a fluid-flow independent mechanism [4]. Future work should focus on model improvements (e.g., laxity and toe-in region of the ligaments, asymmetric material behavior, articular cartilage and synovial fluid of facet joints, and muscle contributions), application of combined/complex loads, and detailed comparisons of the simulated spinal injuries with clinical observations.

In summary, the different initiation sites of spinal injuries observed under LD and HD loading conditions suggest that the rate-dependency exhibited by the material properties of spinal components plays a significant role in the onset of spinal injuries. The rate-dependency of the spinal components should always be implemented in FEA studies applied to research on spinal injuries, especially when designing safety devices or choosing rehabilitation programs. To our knowledge, this added complexity is infrequently employed in FE modeling of the spine and, so, the present work is a significant contribution to this field of study.

Conflict of interest There is no conflict of interest. Authors have not received any payment from industry for conducting this work and are in no conflict of interest.

References

1. Begeman PC, Visarius H, Nolte LP, Prasad P (1994) Viscoelastic shear response of the cadaver and Hybrid III lumbar spine. Presented at the 38th Stapp Car Crash Conference, Fort Lauderdale, FL, USA

2. Demotropoulos CK, Yang KH, Grimm MJ, Artham KK, King AI (1999) High rate mechanical properties of the Hybrid III and cadaveric lumbar spines in flexion and extension. In: 43rd Stapp Car Crash Conference Proceedings, San Diego, California

3. Demotropoulos CK, Yang KH, Grimm MJ, Khalil TB, King AI (1998) Mechanical properties of the cadaveric and Hybrid III lumbar spines. In: 42nd Stapp Car Crash Conference Proceedings, Tempe, Arizona

4. DiSilvestro MR, Suh JK (2001) A cross-validation of the biphasic poroviscoelastic model of articular cartilage in unconfined compression, indentation, and confined compression. J Biomech 34:519–525

5. Duma SM, Kemper AR, McNeely DM, Brolinson PG, Matsuoka F (2006) Biomechanical response of the lumbar spine in dynamic compression. Biomed Sci Instrum 42:476–481

6. El-Rich M, Arnoux PJ, Wagnac E, Brunet C, Aubin CE (2009) Finite element investigation of the loading rate effect on the spinal load-sharing changes under impact conditions. J Biomech 42:1252–1262

7. Fazzalari NL, Parkinson IH, Fogg QA, Sutton-Smith P (2006) Antero-postero differences in cortical thickness and cortical porosity of T12 to L5 vertebral bodies. Joint Bone Spine 73:293–297

8. Garo A, Arnoux PJ, Aubin CE (2009) Estimation of bone material properties using an inverse finite element method. Comput Methods Biomech Biomed Eng 12:121–122

9. Garo A, Arnoux PJ, Wagnac E, Aubin CE (2011) Calibration of the mechanical properties in a finite element model of a lumbar vertebra under dynamic compression up to failure. Med Biol Eng Comput 49:1371–1379

10. Groves CJ, Cassar-Pullicino VN, Tins BJ, Tyrrell PN, McCall IW (2005) Chance-type flexion-distraction injuries in the thoracolumbar spine: MR imaging characteristics. Radiology 236:601–608

11. Haug E, Choi HY, Robin S, Beaugonin M (2004) Human models for crash and impacts simulation. Special volume of Handbook of Numerical Analysis, XII. Elsevier B.V., North Holland

12. Hsu JM, Joseph T, Ellis AM (2003) Thoracolumbar fracture in blunt trauma patients: guidelines for diagnosis and imaging. Injury 34:426–433

13. Imai K, Ohnishi I, Bessho M, Nakamura K (2006) Nonlinear finite element model predicts vertebral bone strength and fracture site. Spine 31:1789–1794

14. Ivancic PC, Coe MP, Ndu AB, Tominaga Y, Carlson EJ, Rubin W et al (2007) Dynamic mechanical properties of intact human cervical spine ligaments. Spine J 7:659–665

15. Kazarian LE, Beers K, Hernandez J (1979) Spinal injuries in the F/FB-111 crew escape system. Aviat Space Environ Med 50:948–957

16. Kemper AR, McNally C, Duma SM (2007) The influence of strain rate on the compressive stiffness properties of human lumbar intervertebral discs. Biomed Sci Instrum 43:176–181

17. Kimura S, Steinbach GC, Watenpaugh DE, Hargens AR (2001) Lumbar spine disc height and curvature responses to an axial load generated by a compression device compatible with magnetic resonance imaging. Spine 26:2596–2600

18. King AI (2002) Injury to the thoracolumbar spine and pelvis. Accidental injury: biomechanics and prevention, 2nd edn. Springer, New York

19. Kosmopoulos V, Keller TS (2003) Finite element modeling of trabecular bone damage. Comput Methods Biomech Biomed Eng 6:209–216

20. Langrana NA, Harten RR, Lin DC, Reiter MF, Lee CK (2002) Acute thoracolumbar burst fractures: a new view of loading mechanisms. Spine 27:498–508

21. Leucht P, Fischer K, Muhr G, Mueller EJ (2009) Epidemiology of traumatic spine fractures. Injury 40:166–172

22. Magerl F, Aebi M, Gertzbein SD, Harms J, Nazarian S (1994) A comprehensive classification of thoracic and lumbar injuries. Eur Spine J 3:184–201

23. Neumann P, Nordwall A, Osvalder AL (1995) Traumatic instability of the lumbar spine. A dynamic in vitro study of flexion-distraction injury. Spine 20:1111–1121

24. Neumann P, Osvalder AL, Hansson TH, Nordwall A (1996) Flexion-distraction injury of the lumbar spine: influence of load, loading rate, and vertebral mineral content. J Spinal Disord 9:89–102

25. Ochia RS, Tencer AF, Ching RP (2003) Effect of loading rate on endplate and vertebral body strength in human lumbar vertebrae. J Biomech 36:1875–1881

26. Oloyede A, Broom ND (1993) A physical model for the time-dependent deformation of articular cartilage. Connect Tissue Res 29:251–261

27. Osvalder AL, Neumann P, Lovsund P, Nordwall A (1993) A method for studying the biomechanical load response of the (in vitro) lumbar spine under dynamic flexion-shear loads. J Biomech 26:1227–1236

28. Pintar FA, Yoganandan N, Myers T, Elhagediab A, Sances A Jr (1992) Biomechanical properties of human lumbar spine ligaments. J Biomech 25:1351–1356

29. Qiu TX, Tan KW, Lee VS, Teo EC (2006) Investigation of thoracolumbar T12–L1 burst fracture mechanism using finite element method. Med Eng Phys 28:656–664

30. Race A, Broom ND, Robertson P (2000) Effect of loading rate and hydration on the mechanical properties of the disc. Spine 25:662–669

31. Roberts S, McCall IW, Menage J, Haddaway MJ, Eisenstein SM (1997) Does the thickness of the vertebral subchondral bone reflect the composition of the intervertebral disc? Eur Spine J 6:385–389

32. Schmidt H, Heuer F, Simon U, Kettler A, Rohlmann A, Claes L et al (2006) Application of a new calibration method for a three-dimensional finite element model of a human lumbar annulus fibrosus. Clin Biomech 21:337–344

33. Schmidt H, Kettler A, Heuer F, Simon U, Claes L, Wilke HJ (2007) Intradiscal pressure, shear strain, and fiber strain in the intervertebral disc under combined loading. Spine 32:748–755

34. Shirado O, Kaneda K, Tadano S, Ishikawa H, McAfee PC, Warden KE (1992) Influence of disc degeneration on mechanism of thoracolumbar burst fractures. Spine 17:286–292

35. Shirazi-Adl A (1994) Biomechanics of the lumbar spine in sagittal/lateral moments. Spine 19:2407–2414

36. Shirazi-Adl A, Ahmed AM, Shrivastava SC (1986) A finite element study of a lumbar motion segment subjected to pure sagittal plane moments. J Biomech 19:331–350

37. Sundgren PC, Philipp M, Maly PV (2007) Spinal trauma. Neuroimaging Clin N Am 17:73–85

38. Tran NT, Watson NA, Tencer AF, Ching RP, Anderson PA (1995) Mechanism of the burst fracture in the thoracolumbar spine. The effect of loading rate. Spine 20:1984–1988

39. Wagnac E, Michardiere D, Garo A, Arnoux PJ, Mac-Thiong JM, Aubin CE (2010) Biomechanical analysis of pedicle screw placement: a feasibility study. Stud Health Technol Inform 158:167–171

40. Wagnac E, Aubin CE, El-Rich M, Arnoux PJ (2011) Finite element modeling of the lumbar spine ligaments for virtual trauma simulations. Med Eng Phys (MEP-D-11-00430)

41. Wagnac E, Aubin CE, Garo A, El-Rich M, Arnoux PJ (2011) Calibration of hyperelastic material properties of the human lumbar intervertebral disc under fast dynamic compressive loads. J Biomech Eng 133:101007

42. White AA, Panjabi MM (1990) Clinical biomechanics of the spine, 2nd edn. J.B. Lippincott, Philadelphia

43. Wilcox RK, Allen DJ, Hall RM, Limb D, Barton DC, Dickson RA (2004) A dynamic investigation of the burst fracture process using a combined experimental and finite element approach. Eur Spine J 13:481–488

44. Yang KH, Hu J, White NA, King AI, Chou CC, Prasad P (2006) Development of numerical models for injury biomechanics research: a review of 50 years of publications in the Stapp Car Crash Conference. Stapp Car Crash J 50:429–490

45. Yingling VR, Callaghan JP, McGill SM (1997) Dynamic loading affects the mechanical properties and failure site of porcine spines. Clin Biomech 12:301–305

46. Yingling VR, McGill SM (1999) Anterior shear of spinal motion segments. Kinematics, kinetics, and resultant injuries observed in a porcine model. Spine 24:1882–1889

47. Zhao FD, Pollintine P, Hole BD, Adams MA, Dolan P (2009) Vertebral fractures usually affect the cranial endplate because it is thinner and supported by less-dense trabecular bone. Bone 44:372–379